Quantitative Raman calibration of sulfate-bearing polymineralic mixtures: a S quantification in sedimentary rocks on Mars

Chloé Larre, Yann Morizet, Catherine Guillot-Deudon, Fabien Baron, Nicolas Mangold

<u>Quantitative Raman calibration of sulfate-bearing polymineralic mixtures: a S quantification in sedimentary rocks on Mars</u>

C. LARRE[1*], Y. MORIZET[1], C. GUILLOT-DEUDON[1,2], F. BARON[1] and N. MANGOLD[1]

[1] Université de Nantes, Faculté des Sciences et Techniques, Laboratoire de Planétologie et Géodynamique (LPG), UMR CNRS 6112, 2 rue de la Houssinière, 44322 Nantes, France

[2] IMN, Institut des Matériaux Jean Rouxel de Nantes, UMR CNRS 6502, 2 rue de la Houssinière, 44322 Nantes, France

* Corresponding author e-mail : chloe.larre@univ-nantes.fr

Abstract

The NASA 2020 Mars mission is a Curiosity-type rover aiming to improve the knowledge of the geologic and climatic evolution of Mars and collect rock samples for future return to Earth. The new rover presents a payload of seven instruments including the SuperCam instrument which is constituted of four tools including a Raman spectrometer. This Raman device will be non-destructive and will analyze the surface remotely in order to determine the mineralogy of rocks and, by extent, to detect and quantify major elements such as sulfur. Sulfur has been detected under sulfate forms (Ca,Mg,Fe-sulfates) in sedimentary rocks. This element is difficult to quantify

using the laser ablation tool of the ChemCam instrument onboard the Curiosity rover.

We propose a Raman calibration to constrain the sulfur abundance in multi-minerallic mixtures.. We acquired Raman signatures on binary and ternary mechanical mixtures containing Ca and Mg sulfates, mixed with natural silicate minerals: olivine, clinopyroxene, orthopyroxene and plagioclase; and supposed to be relevant of basaltic-sedimentary rocks at the surface of Mars. Specific processing of Raman spectra extracted from our mixtures using Voigt function allows us to recover the initial proportions of our preparations on Ca and Mg sulfates. From these simulations, calibration equations have been provided allowing us to determine sulfate proportions ($CaSO_4$ and $MgSO_4$) in a mixture with basaltic minerals. With the presented calibration, S can be quantified at a lower limit of 0.7 wt % in martian soil.

1. Introduction

One of the main objectives of both orbital and landed Mars missions is the mineralogical characterization of the igneous and sedimentary rocks in order to constrain past geological processes such as the early volcanism and aqueous alteration. So far, many igneous rocks have been detected at the surface of Mars and basaltic rocks represent the

most abundant part (e.g., Bandfield et al. 2000; McSween et al. 2009; Taylor and McLennan 2009; Ody 2012; Baratoux et al. 2013; Sautter et al. 2016; Cousin et al. 2017). Although the Curiosity rover and the orbital spectrometer CRISM have recently discovered more felsic and alkali-rich rocks including trachyte, andesite, diorite and putative granitoïds (Wray et al. 2010; Stolper et al. 2013; Sautter et al. 2015; Mangold et al. 2016). These magmatic rocks have been altered into various minerals such as clays (various smectites, kaolinite, chlorite), sulfates (Ca-, Fe-, Mg-sulfates), which are often detected in sediment layers overlying the igneous bedrock or in crustal outcrops exhumed by impact craters (e.g., Squyres et al. 2004; Arvidson et al. 2005; Poulet et al. 2005; Gendrin et al. 2005; Elhmann et al. 2013, Carter et al. 2013).

The Curiosity rover currently analyzes rocks and soils on Mars using Laser Induced Breakdown Spectroscopy (LIBS) (Maurice et al. 2012; Wiens et al. 2012; Meslin et al. 2013; Maurice et al. 2017; Cousin et al. 2017; Mangold et al. 2017). The LIBS equipment enables the detection and quantification of all major elements (e.g., Si, Al) and the detection of volatiles and halogens (C-H-O-N-P-S-F-Cl). However, the detection of these elements is difficult with this method because of the high excitation energies, their peak positions near the instrument limit and the coupling of different major elements rays (e.g. Sallé et al. 2004, Clegg et al. 2007). This results in varying detection levels and lack of quantification for some of them. In particular, the detection limit for S is of 5 to 10 wt% S (Wiens et al. 2012). Quantitative determination of

71   S is of prime interest, as this element is known to be fundamental for

72   Mars evolution (King and McLennan 2010).

73   In the future Mars 2020 mission, the SuperCam analytical equipment

74   will include Raman and IR spectrometers in addition to the LIBS

75   instrument similar to ChemCam instrument onboard Curiosity (Fouchet

76   et al. 2016; Wiens et al. 2016, Ollila et al. 2017). Relevant

77   interpretations of Raman spectra will require the acquisition of

78   laboratory data under similar analytical conditions of the Raman

79   spectrometer onboard. Although Raman spectroscopy is nominally

80   non-quantitative with relevant calibration, it can be used for quantifying

81   S at low concentrations (thousands of ppm) owing to the high Raman

82   activity of S-bearing molecular groups (Morizet et al. 2017).

83   Previous studies have focused on the quantification of volatile species

84   (H_2O, CO_2 and SO_4^{2-}) in silicate glasses with application to Earth

85   volcanism (Zajacz et al. 2005; Mercier et al. 2009; Le Losq et al. 2012;

86   Morizet et al. 2013, 2017). However, up to now, the quantification of

87   individual mineral species in multi-minerallic mechanical mixtures

88   have been merely addressed using Raman spectroscopy (Kontoyannis

89   et al. 1997; Jehlicka et al. 2009; Noguchi et al. 2009; Kriskova et al.

90   2013). Jehlicka et al. (2009) have shown, the possibility to quantify

91   multi-component mixtures with a portable micro-Raman spectrometer.

92   In Kriskova et al. (2013) and Noguchi et al. (2009) only multi-

93   minerallic mixtures with carbonates have been studied. Kontoyannis et

94   al. (1997) have established a calibration on carbonates mixed with

4

95 gypsum using Raman spectroscopy, but not applied to mineralogical

96 mixtures representative of Mars mineralogy.

97 In the present work, we propose a calibration for quantifying the sulfate

98 content (thereby also the elemental sulfur content) in multi-minerallic

99 mixtures. This calibration aims to be subsequently applied for

100 quantifying S under its sulfate form on the surface of Mars with the

101 Raman spectrometer of SuperCam. Several mixtures of sulfates (Ca-

102 sulfate, Mg-sulfate) with silicate minerals (i.e., pyroxenes, olivine, and

103 plagioclase) were prepared in order to reproduce sulfate-bearing

104 Martian-like sedimentary rocks. These mixtures were analyzed by

105 Raman spectroscopy. The equations derived from calibration curves are

106 then used to quantity sulfates in these mixtures. Finally, we discuss the

107 potential of this method to quantify S carried by sulfates in the Martian

108 soil and rocks.

109

110 **2. Methods**

111 *2.1. Multi-minerallic mixtures preparation:*

112 Multi-minerallic   mixtures   were   prepared   from   Ca-sulfate

113 ($CaSO_4.2H_2O$) and Mg-sulfate ($MgSO_4.nH_2O$) synthetic powders and

114 silicate minerals selected from natural rocks. Pyroxenes and olivine

115 were extracted from a xenolith collected at the maar of Borée (France)

116 and plagioclase from a norite of Stillwater (USA). Chemical

117 compositions of minerals selected for this study are reported in Table

118 1. Olivine is Mg-rich in composition (forsterite, $Si_{1.00}$ $Fe_{0.18}$ $Mg_{1.78}$

5

119    $Na_{0.01} O_4$).Pyroxenes have compositions close to enstatite ($Si_{1.85} Al_{0.16}$

120    $Fe_{0.16} Mg_{1.62} Ca_{0.02} Na_{0.02} O_6$) and augite end-members ($Si_{1.78} Al_{0.23} Fe_{0.09}$

121    $Mg_{0.95} Ca_{0.57} Na_{0.11} O_6$). The plagioclase from this study is Ca-rich and

122   has composition close to the anorthite end-member ($Si_{2.21} Al_{1.76} Fe_{0.01}$

123    $Mg_{0.01} Ca_{0.85} Na_{0.16} O_8$). Natural silicate minerals were crushed in a

124   steel-mortar with pestle and crushed again in an agate mortar. Ethanol

125   was added during crushing to clean the samples.

126   Mixtures between silicate minerals and sulfates were prepared and

127   mixed in together. The resulting powder was not sieved because grain

128   size does not exceed 50 µm with this grinding procedure (see Figure

129   1A). Several samples at various sulfate proportions were prepared:

130    $WF_{gypsum} = 0.20, 0.10, 0.05, 0.03, 0.01$ and $WF_{mg\text{-}sulfate} = 0.20, 0.10, 0.05$

131   and 0.03; where WF represents the Weight Fraction of sulfates. Ternary

132   mixtures were prepared with Ca-sulfate, clinopyroxene and olivine.

133   Gypsum, clinopyroxene and olivine concentrations in mixtures were

134   respectively: $WF_{gypsum} = 0.20, 0.10$ and 0.05, $WF_{clinopyroxene} = 0.40, 0.40$

135   and 0.45, $WF_{olivine} = 0.40, 0.50$ and 0.50. The investigated sulfate

136   concentrations are consistent with the abundances of these minerals as

137   locally estimated in evaporites at Meridiani Planum (McLennan et al.

138   2006) or in fluvio-lacustrine sedimentary rocks at Gale crater (Vaniman

139   et al. 2017).

140   We also prepared ternary mixtures in order to reproduce in a more

141   realistic system the suggested Martian surface mineralogy: sulfates

142   mixed silicate minerals resulting of basalt alteration (Carter et al. 2013;

6

143   Forni et al. 2015; Cousin et al. 2017; Mangold et al. 2017). The resulting

144   powders were then pressed into pellets (Figure 1A). Pressures used

145   were between 5,000 and 9,000 kg/cm^2 to create pellets with 7 to 10 mm

146   in diameters, respectively.

147

148   *2.2. Raman spectroscopy*

149   The non-destructive nature of the Raman analyses will allow

150   mineralogical characterization (e.g., Reynard et al. 2012) of the Martian

151   rocks without any sample preparation. The Raman spectroscopy uses a

152   laser with a specific wavelength, which will excite molecules (Brawer

153   and White 1975; Mysen and Virgo 1980a, b; McMillan 1984; Rossano

154   and Mysen 2009; Rull 2012). The excitation of molecules produces a

155   Raman shift (i.e., the wavenumber differences between the signal from

156   the laser and the response of excited molecules;Delhaye and

157   Dhamelincourt 1975; Hoehse et al. 2009; Dubessy et al. 2012). The

158   strongest signatures received and detected by the Raman spectrometer

159   are called ν_1 signatures and correspond to the symmetric stretching of

160   the molecules excited by the laser (Rossano and Mysen 2009; Rull

161   2012).

162   Raman spectra for each pellet were acquired on a Jobin-Yvon Labram

163   HR800 spectrometer equipped with a solid state laser diode operating

164   at 532 nm. A 20X Olympus objective was used. A 785 nm solid state

165   laser has also been used on one sample (GPG80, plagioclase-gypsum

166   mixture with $WF_{gypsum} = 0.20$) to circumvent the fluorescence. Spectra

are acquired with a 300 grooves/mm grating with a 3 cm^{-1} spectral resolution. The output power of the laser was set to 74 mW for Ca-sulfate mixtures and 50 mW for Mg-sulfate. For binary mixtures, we did not use the confocal mode (with a hole calibrated around 50 µm) and the hole was fixed at 200 µm. However, ternary mixtures were analyzed in a confocal mode due to fluorescence problems (Panzcer et al. 2012) in the non-confocal configuration.

The acquisition time varied from 3 to 10 s and 3 repetitive scans were made on each point. Backgroun substraction for each spectrum has been applied following the procedure of Tarcea and Popp (2012): a fit of polylines (i.e., multiple lines added to create a baseline under the spectrum) was made for each spectrum to establish a baseline correction in order to measure areas and intensities for each peak. Peak intensity and area were determined on normalized spectra to the same acquisition time length (10 or 15 s). Details of the analytical conditions are reported in the Supplementary Material (Table 1).

A large mapping of 5 by 5 mm (Figure 1B) was conducted on each pellet with a spot size of about 1.6 µm. Each analyses were performed every 150 µm.This mapping results in 1024 spectra representing the mixture analyzed. Since grain size did not exceed 50 µm, possible coupling of the same crystal analysis is expected. This phenomenon would have occurred for every crystal, since we suppose the mixture homogeneous in grain size (Figure 1A). Then, an average of these spectra, that will consider the previous artefact, is computed to obtain a

191   single Raman spectrum representative of the analyzed mixture (Figure

192   1C).

193   The effect of polarization was also tested on Raman spectra of pure

194   minerals. We have observed that the spectrum intensity is modified

195   when acquisition angle on the crystal is changed, which is consistent

196   with the results of Bremard et al. (1986) and Rull (2012) where

197   polarization effects have been observed and measured when changing

198   crystal orientation. Nevertheless, we assumed that the polarization

199   effect is averaged out by the large mapping procedure adopted and

200   considering that crystals in the pellet have all possible crystallographic

201   orientations from a statistical point of view.

202   *2.2.1 Mineral Raman spectra:*

203   The Raman spectrum of each individual mineral used in this study is

204   reported in Figure 2. The gypsum Raman pure spectrum (Figure 2A)

205   exhibits several peaks with low intensities in the 400-700 cm^{-1} region

206   corresponding to the symmetric (400-500 cm^{-1}) and antisymmetric

207   (600-700 cm^{-1}) bending vibrations of SO_4 molecules (ν_2 and ν_4). The

208   strong peak at 1006 cm^{-1} corresponds to the symmetric stretching

209   vibration (or ν_1) of S-O bonds in SO_4 molecular groups (Knittle et al.

210   2001; Buzgar et al. 2009; Bishop et al. 2014). Peaks observed in the

211   highest frequency region (> 1100 cm^{-1}) are attributed to antisymmetric

212   stretch vibrations (ν_3) of SO_4 and have a weak Raman activity.

213   Similar to gypsum, the principal symmetric ν_1 vibration of Mg-

214   sulfate is identified in Figure 2B around 1040 cm^{-1} (Buzgar et al. 2009).

9

215   Antisymmetric bending and stretching of SO_4 molecules are observed

216   at 620 and 1110 cm^{-1}, respectively.

217   The Raman spectrum of olivine (Figure 2C) shows two strong peaks

218   above 800 cm^{-1}, followed by two less intense peaks above 900 cm^{-1},

219   which are attributed to the symmetric stretch of the Si-O bonds of SiO_4

220   tetrahedrons (Chopelas 1991; Kolesov and Tanskaya 1996; Kolesov

221   and Geiger 2004; Kuebler et al. 2006; McKeown et al 2010).

222   Plagioclase Raman spectrum shown in Figure 2D exhibits a strong

223   peak around 500 cm^{-1} attributed to the ν_1 of Al_2O_3 or SiO_4 tetrahedrons

224   in the tectosilicate structure (Sharma et al. 1983; Freeman et al. 2008).

225   Peaks identified at higher wavenumbers correspond to the ν_3 vibrations

226   for these tetrahedrons.

227   Pyroxenes spectra shown in Figures 2E and 2F are similar in the high

228   frequency region (> 600 cm^{-1}) where bending and stretching vibrations

229   of SiO_4 tetrahedrons are observed, for signatures around 660 and 1006

230   cm^{-1} respectively. At low frequency, in the 200-400 cm^{-1} region, it is

231   possible to discriminate clinopyroxene from orthopyroxene, which does

232   not present the same peak intensities. In this region, vibrations related

233   to Fe, Ca and Mg molecular environments are responsible for the

234   observed peaks (Sharma et al. 1983; Huang et al. 2000; Wang et al.

235   2001; Prencipe et al. 2011). Specific peak assignments for each mineral

236   in this study are described in Table 2.

237   *2.2.2. Analytical conditions useable for the SuperCam instrument:*

10

The new rover send for the 2020 Mars mission will use a laser-pulse Raman spectrometer with a 532 nm solid-state laser (Olila et al. 2012, Wiens et al. 2016). The rover will target rocks and soil from several meters away and with a resolution on the order of 10 cm^{-1} (Wiens et al. 2016).

Knowing those conditions, we performed several tests to analyze the pellets. A map size of 5 by 5 mm was necessary to reproduce in an adequate way the mineral mixtures. Using 2 by 2 or 3 by 3 mm map size was not sufficient to retrieve the initial mineral proportions in the mixture. Furthermore, the 5 by 5 mm size map is also consistent with the analytical conditions for the 2020 rover, which will have a large analytical area. The adopted laboratory analytical conditions (i.e., focus 20X, 300 grooves/mm grating and non-confocal mode) were optimized to obtained spectra that could be compared to the Raman spectra which will be acquired by SuperCam.

2.3. Calibration method:

The calibration method in the present study is similar to that used by Kontoyannis et al. (1997), Noguchi et al. (2009) and Kristova et al. (2013). Our method is based on the spectral deconvolution of the investigated pure minerals Raman spectrum presented in the previous section. For instance, to establish a calibration on a gypsum-olivine mixture, pure spectrum of gypsum and olivine are treated individually. The spectrum treatment consists in extracting peak information using

262   subsequent deconvolution. Since we are analyzing crystallized species,

263   we expect the Raman signature to have a pure Lorentzian shape;

264   however, a contribution of a Gaussian component in addition to the

265   Lorentzian signal has been observed. This would likely be caused by

266   intrinsic crystal defaults. Therefore, we used a Voigt simulation (i.e., a

267   mix of Gaussian and Lorentzian deconvolution) which provides better

268   simulations of our spectra. The simulation equation of a Voigt

269   deconvolution is given below (Eq.1):

270

$$y = y_0 + A \; \frac{2 \ln 2}{\pi^{\frac{3}{2}}} \times \frac{W_L}{W_G^2} \times \int_{-\infty}^{\infty} \frac{e^{-t^2}}{\left(\sqrt{\ln 2} \times \frac{W_L}{W_G}\right)^2 + (\sqrt{4 \ln 2} \times \frac{x - x_c}{W_G} - t)^2} \, dt \qquad (1)$$

271   Where y_0 and y are the intensity after a baseline correction of the

272   spectrum and the intensity for the peak simulated, respectively. The

273   parameter A represents the simulated area and W_G et W_L are

274   respectively the Gaussian and Lorentzian widths for a given peak. The

275   x parameter is the position in cm^{-1}; where x is the Raman shift and x_c is

276   the derived peak position simulated in cm^{-1}. Finally, in Eq. 1, t is the

277   time component. Since the Raman spectra are not time-dependent, t is

278   set to 0. We reported in the Supplementary Material (Table 1) all peaks

279   simulated for mineral pure spectrum, with their specifics parameters

280   (width, position, area). Forclarity, simulations of silicate and sulfate

281   minerals pure spectra are only shown in the Supplementary material

282   (Fig.S1).

283   Due to the strong overlapping between the different spectral lines in the

284   recoveredaverage Raman spectrum for each pellet, it was not possible

285   to perform the simulation of all the identified peaks for pure spectrum

286   of minerals reported in Table 2. For instance, clinopyroxene has a main

287   peak at 1006 cm^{-1} comparable to the one in gypsum Raman spectrum.

288   Therefore, simulating those two peaks in the average mixed spectrum

289   is complicated by their proximity and relevant simulation could not be

290   achieved. Hence, for each species, we have selected peaks that are

291   distinct in their position and indicated in Table 3.

292   The protocol to simulate Raman peaks is fully described in previous

293   studies and is routinely used for the quantification of volatiles species

294   in silicate glasses (Mysen and Virgo 1980a, b; Mercier et al. 2009;

295   Morizet et al. 2013, 2017). First, we have fixed the peak position and

296   widths (Gaussian and Lorentzian), leaving only the peak area

297   optimized. Position is then optimized as we observed slight variations

298   in the peak position in our mixture spectrum compared to the position

299   derived from the acquired pure spectrum. These variations could be due

300   to the dependence of the Raman signature on crystal orientation or

301   unaccounted chemical heterogeneity. Gaussian and Lorentzian widths

302   are also optimized to better adjust our simulations. This procedure is

303   repeated several times until the chi-square (χ^2 parameter representing

304   the robustness of the fit) is the lowest possible and the residual are small

305   (see Figure 3).

306   With parameters extracted from simulations, we were able to calculate

307   the mixing proportion present in the analyzed pellet. We determined a

308   ratio R between the simulated area for the peak of the mixed spectrum

309   and that of the pure spectrum such as:

13

$$R = \frac{A_{mixture}}{A_{pure}} \quad (2)$$

In Eq.2, A represents the area determined with a Voigt simulation for a same peak for the mixture ($A_{mixture}$) and the pure Raman spectrum (A_{pure}). This method differs from previous Raman calibrations studies of Kontoyannis et al. (1997) and Kriskova et al. (2013) where peak intensities were chosen instead of areas. Since we observed several variations in intensity and peak positions between pure spectrum and the average spectrum of the mixture, we consider that peak areas averaged out every possible variation between acquisitions with the 300 grooves/mm grating. The ratios are then normalized to obtain the result in weight fraction (WF). This proportion is then assimilated to a coefficient "a":

$$a = \frac{\Sigma A_{gypsum}}{\Sigma A_{mineral}} \quad (3)$$

with A being peak areas for gypsum (A_{gypsum}) and for mineral in the mixture ($A_{mineral}$). In case of the ternary mixtures with more than 2 peaks simulated for one mineral, $A_{mineral}$ is entirely summed in the denominator. Examples of mineral pure spectrum and mixture deconvolutions are provided in the Supplementary Material (Fig.S1).

3. Results

3.1. Binary and ternary mixtures with Ca-sulfate:

A typical example of the spectral treatment is presented in Figure 3. In Figure 3A, Raman spectra collected represents olivine and gypsum

14

mixtures with: WF_{gypsum} = 0.2, 0.1, 0.05 and 0.01. The Raman spectra obtained for the mixtures with other minerals (pyroxenes and plagioclase) are reported in the Supplementary Material (Fig.S2). In Figure 3A, it can be observed that the peak intensity for ν_1 gypsum at 1006 cm^{-1} increases with increasing the proportion of gypsum in the mixture. For instance, in GOLI80 WF_{gypsum} = 0.20 (see Table 3 for theoretical WF of each mixture), the 1006 cm^{-1} symmetric stretch peak is more intense as compared to the one in GOLI90 (WF_{gypsum}= 0.10). For these two mixtures, the measured intensity in the SO_4 vibrations peak is twice for GOLI80 as compared to the one in GOLI90 which appears to be consistent with the prepared compositions (Table 3). Although the gypsum content in the GOLI99 mixture is extremely low (WF_{gypsum} = 0.01), the peak at 1006 cm^{-1} is still detected because of the strong Raman activity of symmetric stretch of the S-O bonds in SO_4 molecular groups in gypsum (see Figure 3A).

We chose to simulate three different peaks in the 890-1100 cm^{-1} region and located at 914, 958 for olivine and 1006 cm^{-1} for gypsum (Figure 3). For on olivine mixtures, relevant results were obtained when considering two Raman peaks identified in Table 2: 914 cm^{-1} for olivine and 1006 cm^{-1} for gypsum. In order to avoid contribution of the 1006 cm^{-1} gypsum peak over the 950 cm^{-1} of olivine (see on Figure 3E-H), we have simulatedthe olivine peak at 914 cm^{-1} for our simulations. The robustness of our simulations is asserted by the small residual observed in Figure 3E-H. For a theoretical proportion mixture of 0.80 and 0.20 weight fraction of olivine and gypsum respectively (Figure 3D), the

15

358 calculated proportions (from Eq. 2 and 3) are 0.79 (0.08, error relative

359 to simulations) for olivine and 0.21 (0.01) for gypsum (Figure 3H).

360 With lower Ca-sulfate proportion, we obtain consistent results in

361 between the measured and theoretical mixtures. For initial proportions

362 at 0.90 and 0.10, we calculate 0.91 (0.01) for olivine and 0.09 (0) for

363 gypsum (Figure 3C and 3G). The same applies with the 0.01 and 0.05

364 mixtures of gypsum where 0.01 (0.01) and 0.06 (0) weight fraction of

365 gypsum is calculated respectively, as shown in Figure 3A,B and Figure

366 3E,F.

367 On the Figure 4 is showed the calculated coefficients from simulated

368 areas in each mixture (see Eq.3) as a function of the theoretical $CaSO_4$

369 content. The results are represented for the different mixtures with

370 basaltic minerals: plagioclase-gypsum mixture in Figure 4A,

371 orthopyroxene-gypsum in Figure 4B, clinopyroxene and olivine-

372 gypsum in Figure 4C and 4D, respectively. Results from simulations

373 are reported in Table 3. In Figure 4, we can observe that the best

374 calibration (based on the linear regression coefficient R^2 which defines

375 the quality of the linear regression on experimental data) is obtained for

376 olivine-gypsum simulations comparing to the calibration with other

377 silicate minerals. Simulations (Figures 4A to 4C) show good R^2 with

378 0.95, 0.94 and 0.96 for plagioclase, orthopyroxene and clinopyroxene

379 respectively. The plagioclase-mixture with 0.20 weight fraction of

380 gypsum (i.e., GPG80, see Table 3) has been calibrated using different

381 peaks because of the use of the 785 nm laser for our analysis.

382 Consequently, this point is not reported in Figure 4A.

16

We adopted the same procedure as for binary mixtures for ternary mixtures. The retained peak positions for our simulations are reported in Table 3. We considered the 300-390 cm^{-1} clinopyroxene peak areas, representative of Ca-O stretching vibrations, since they are isolated from the contribution of olivine and gypsum peaks in the Raman spectrum. For olivine, we consider the 947 cm^{-1}, one of SiO$_4$ symmetric stretching vibrations signatures, and 485 cm^{-1} for gypsum which represents the bending of SO$_4$ molecules. Those peaks were selected because they were the most separated from each other.

Simulations results and derived coefficients are reported in Table 3. We established a calibration expressed with the coefficient calculated (Eq.3) from areas simulated for each mineral according to the initial weight fraction of gypsum, indicated in Figure 5. In the Figure 5, we obtained a good calibration with R^2 = 0.99 on ternary mixtures.

3.4. Binary mixtures with Mg-sulfate

As for Ca-sulfate mixtures, we proceeded with the same method for pellets containing Mg-sulfate. We reported results from Mg-sulfate calibration on Figure 6 where the same mixtures of natural silicate minerals of olivine, pyroxenes and plagioclase are represented. In Figures 6A and 6C, pyroxenes calibration with Mg-sulfate are showed. As we can see on these results, the R^2 is fairly good (0.86 for orthopyroxene mixtures and 0.85 for clinopyroxene) and initial proportions of Mg-sulfate can be well estimatedfrom our method.

17

407   Plagioclase mixtures with Mg-sulfate is reported on Figure 6B, where

408   we obtained $R^2=0.43$ and show the less consistent results. Finally,

409   olivine mixtures with initial proportions of Mg-sulfate (Figure 6D)

410   result in a $R^2=0.69$. All results of calculated mixtures proportions are

411   reported in Table 3.

412

413   **4. Discussion**

414   Binary and ternary mixtures with sulfates were calibrated with several

415   proportions of sulfate tested. In this section, we discuss the limit of our

416   calibration method and its application to the martian context.

417   *4.1. Detection limit of sulfur:*

418   In Figure 4 we have reported results from binary mixtures of gypsum.

419   We reported error bars extracted from errors under peak areas

420   simulated. As can be observed in Figures 4B and 4C, corresponding to

421   pyroxene-bearing mixtures, samples with 0.03 and 0.01 weight

422   fractions of gypsum present a significant vertical error. Some selected

423   peaks for the calibration do not exhibit a high Raman activity but we

424   had to select those peaks, , due to the necessity of choosing individual

425   peaks for our simulations. In simulation results shown in Table 3, we

426   can see that we have still a good agreement in between the calculated

427   proportions and the initial proportions within the mixtures. Considering

428   that some of molecule vibrations are less Raman active relative to

429   Raman spectroscopy, we consider that our method of calibration is

430   reliable until $WF_{sulfate}= 0.03$ weight fraction in a mechanical mixture.

18

Knowing this detection limit of our calibration, we can extrapolate this method to Martian rocks. With the proposed method and the calibration equations, S could be determined at the surface of Mars for a sedimentary rock containing sulfate until approximately $WF_S = 0.007$ weight fraction (i.e., 7 000 ppm). Below this S content, our calibration can still beapplied, but the errors will be higher and results might not be reliable.

4.2. Application to the calibration curves to the determination of sulfur on the Martian surface

Results provided by the calibration are specified in Figure 7 for all mixtures created. On Figure 7, we can see the good agreement of our calibration method. This plot showed us that the calculated proportions of gypsum areclose to the theoretical proportions and all data points are aligned along the 1:1 line. Ternary mixtures with gypsum are also represented and are in good accordance. Mg-sulfate mixtures in Figure 7 showed us that the calibration is also good and data points are aligned along the 1:1 line.

We have reported on Table 3, all calibrations equations calculated from our calibration method for gypsum and Mg-sulfate mixtures.

As a result, we can determine the sulfate content in a mixture with olivine, pyroxenes and plagioclase in unknown proportions according to equations extracted from our simulations shown in Figures 4, 5 and 6. Using a Raman spectrum obtained on the surface of Mars of a

19

455   mechanical solid mixture containing sulfate (Ca or Mg), and simulating

456   specific peaks (reported in Table 3), a coefficient can be calculated (i.e.,

457   the "a" component in equations in Table 3).

458   The established calibration method based on Raman spectroscopy will

459   be of use for the future 2020 Mars mission to quantify S abundance

460   when present as sulfates. For the application of the present calibration,

461   the peak selections from Raman spectrum must be conducted with care.

462   We suggest using only the peaks mentioned in the present work and

463   reported in the Supplementary Material (Table 1). However, this will

464   be dependent on the resolution of the SuperCam Raman spectrometer

465   and the quality of the acquired signal (Wiens et al. 2016). In the case of

466   a low resolution, peaks with low intensities (for instance ν_3) will be

467   difficult to constrain. However, other peaks mentioned in the

468   Supplementary Material (Table 1), such as ν_1 or ν_2 can be well defined

469   by the future rover and calibration can still be applicable (referred with

470   the Table 1 in the Supplementary Material peak information). Since our

471   analyses were performed with a high resolution Raman spectrometer,

472   further analyses will be acquired with a pulsed-Raman with distance

473   from the sample similar to the one presupposed for SuperCam in order

474   to compare data and modify, if necessary, the calibration.

475   Furthermore, Mars mineralogy has been partly investigated using

476   remote sensing and rover data, as well as Martian meteorites, showing

477   that pigeonite and augite are the two most common pyroxenes found in

478   Martian rocks (both are clinopyroxenes but with low Ca content for

479   pigeonite) (e.g., Lodders 1998, Agee et al. 2004; Mustard et al. 2005;

Cousin et al. 2017; Morrison et al. 2017). Mg-rich olivine, orthopyroxene and plagioclase have also been detected in Martian meteorites and at the surface of the planet(Agee et al. 2004; Mustard et al. 2005; Dehouck et al. 2014; Cousin et al. 2017; Morrison et al. 2017). Nonetheless, Fe-rich olivine can be expected in small amounts which only differs in spectral signature by the relative intensity between the double peak around 800-850 cm^{-1}. Since our calibration is not based on those peaks (see Table 3), the quantification of sulfate with fayalite can still be possible. Plagioclase such as anorthite may be the most common feldspar on Mars (Bish et al. 2013, Blake et al. 2013, Vaniman et al. 2014) although andesine has been observed as the predominant plagioclase at Gale crater by the Curiosity rover instruments (Sautter et al. 2016, Morrison et al. 2017). Consequently, the proposed calibration method can be useable for a mixture of sedimentary rocks containing sulfates and silicate minerals even if the minerals present does not have the same chemical composition within a solid solution as used in our study.

5. Summary

In the present study, we have prepared pellets by mixing Ca and Mg sulfates with silicate minerals commonly found in basalt (olivine, pyroxenes and plagioclase) in order to investigate the Raman signature of multi-minerallic mechanical assemblages. The main objective was to establish a relevant calibration for the determination of S content at the

21

surface of Mars with analytical conditions close to the future Raman spectrometer on SuperCam equipment for the 2020 spatial mission. Calibration equations were obtained for both binary and ternary mixtures of $CaSO_4$ with minerals for a range of gypsum of 0.01 to 0.20 weight fraction. Equations were also estimated from Mg-sulfate mixtures with initial proportion of 0.03 to 0.20 weight fraction.

The protocol used in this study involves simulations of the resulting average Raman spectrum using a Voigt distribution on peaks attributed to each mineral. The simulation of the entire Raman spectrum is not simulated with an enough good accuracy and careful attention is necessary for peak identifications. The actual method could be applied to the quantitative characterization of the soil of Mars which is recognized to present sedimentary rocks containing sulfates and silicate minerals obtained from bedrock erosion.

Given our equations extracted from calibrations on both Mg and Ca sulfates, we would be able to calculate a coefficient from a given Raman spectrum acquired on Mars and treated according to specific peak simulations. Coupling this coefficient with the proper calibration equation (i.e., when knowing the mineralogical characterization of the mixture analyzed) we can estimate the proportion of this sulfate in weight fraction. By extent, this calibration could be used to constraint part of the S content at the surface carried by sulfate minerals phases. We have estimated the detection limit of S at 7 000 ppm which is well below the current detection limit by the LIBS technique (e.g., Wiens et al. 2012; Nachon et al. 2014, Anderson et al. 2017). Nevertheless,

22

further calibrations are requested involving more complex mineral
mixtures, including other sulfates (Fe-sulfate) and sulfides, and
mixtures with more than four compounds.

References

Agee, C.B., Draper, D.S. (2004): Experimental constraints on the origin
of Martian meteorites and the composition of the Martian mantle.
Earth Planet Science Letters, **224**, 415-429.

Anderson, D.E., *et al.* (2017): Characterization of LIBS estimation lines
for the identification of chlorides, carbonates, and sulfates in
salt/basalt mixtures for the application to MSL ChemCam data.
Journal of Geophysical Research: Planets, **122**, 744-770.

550   Arvidson, R.E., Poulet, F., Bibring, J.-P., Wolff, M., Gendrin, A.,

551   Morris, R.V., Freeman, J.J., Langevin, Y., Mangold, N., Bellucci,

552   G. (2005): Spectral reflectance and morphologic correlations in

553   Eastern Terra Meridiani, Mars. *Science*, **307**, 1591-1594.

554   Bandfield, J.L., Hamilton, V.E., Christensen, P.R. (2000): A global

555   view of Martian surface composition from MGS-TES. *Science*,

556   **287**, 1626-1630.

557   Baratoux, D., Toplis, M.J., Monnereau, M., Sautter, V. (2013): The

558   petrogical expression of early Mars volcanism. *Journal of*

559   *Geophysical Research: Planets*, **118**, 59-64.

560   Bish, D.L., et al. (2013): X-ray diffraction results from Mars Science

561   Laboratory: Mineralogy of Rocknest at Gale Crater. *Science*, **341**,

562   3153.

563   Bishop, J.L., Lane, M.D., Dyar, M.D., King, S.J., Brown, A.J., and

564   Swayze, G. (2013): Spectral properties of Ca-sulfates: Gypsum,

565   Bassanite and Anhydrite. *American Mineralogist*, **99**, 2105-2115.

566   Blake, D.F., et al. (2013): Curiosity at Gale crater, Mars:

567   Characterization and analysis of the Rocknest sand shadow.

568   *Science*, **341**, 6153.

569   Bremard, C., Dhamelincourt, P., Laureyns, J., Turrell, G. (1986):

570   Polarization measurements in micro-Raman and

24

microfluorescence spectrometries. *Journal of Molecular Structure*, **142**, 13-16.

Buzgar, N., Buzatu, A., and Sanislav, I.V. (2009): The Raman study on certain sulfates. ANALELE ȘTIINȚIFICE ALE UNIVERSITĂȚII „AL. I. CUZA" IAȘI Geologie. Tomul LV, nr.1.

Carter, J., Poulet, F., Bibring, J.-P., Mangold, N., and Murchie, S. (2013): Hydrous minerals on Mars as seen by the CRISM and OMEGA imaging spectrometers: Updated global view. *Journal of Geophysical Research: Planets*, **118**, 1-28.

Chopelas, A. (1991): Single crystal Raman spectra of forsterite, fayalite, and monticellite. *American Mineralogist*, **76**, 1101-1109.

Clegg, S.M. et al. (2007) : Sulfur geochemical nalysis with remote laser-induced breakdown spectroscopy on the 2009 mars science laboratory rover. *Lunar Planetary Science* Conference abstract #1960.

Cousin, A., Sautter, V., Payré, V., Forni, O., Mangold, N., Gasnault, O., Le Deit, L., Johnson, J., Maurice, S., Salvatore, M., Wiens, R.C., Gasda, P., Rapin, W. (2017): Classification of igneous rocks analyzed by ChemCam at Gale Crater, Mars. *Icarus*, **288**, 265-283.

25

592   Culka, A., Kosek, F., Drahota, P., Jehlicka, J. (2014): Use of
593   miniaturized Raman spectrometer for detection of sulfates of
594   different hydration states – Significance for Mars studies. *Icarus*,
595   **243**, 440-453.

596   Daniel, I. and Edwards, H.G.M. (2012): Raman spectroscopy in
597   biogeology and astrobiology. *EMU Notes in Mineralogy*, **12**, 389-
598   412.

599   Dehouck, E., McLennan, S.M., Meslin, P.-Y., Cousin, A. (2014):
600   Constraints on abundance, composition, and nature of X-ray
601   amorphous components of soils and rocks at Gale crater, Mars.
602   *Journal of Geophysical Research: Planets*, **119**, 2640-2657.

603   Delhaye, M., and Dhamelincourt, P. (1975): Raman microprobe and
604   microscope with laser excitation. *Journal of Raman spectroscopy*,
605   **3**, 33-43.

606   Dubessy, J., Caumon, M.-C., Rull, F., and Sharma, S. (2012):
607   Instrumentation in Raman spectroscopy: elementary theory and
608   practice. *EMU Notes in Mineralogy*, **12**, 83-172.

609   Filiberto, J., Baratoux, D., Beaty, D., Breuer, D., Farcy, B.J., Grott, M.,
610   Jones, J.H., Kiefer, W.S., Mane, P., McCubbin, F.M., Schwenzer,
611   P. (2016): A review of volatiles in the Martian interior.
612   *Meteoritics & Planetary Science*, 1-24.

Forni, O *et al.* (2015): First detection of fluorine on Mars: Implications for Gale Crater's geochemistry. *Geophysical Research Letters*, **42**, 1020-1028.

Fouchet, T., et al. (2016): The SuperCam Remote Sensig Suite for MARS 2020: Nested and Co-Aligned LIBS, Raman, and VISIR Spectroscopies, and color micro-imaging. *American Astronimical Society*.

Freeman, J.J., Wang, A., Kuebler, K.E., Jolliff, D.L., Haskin, L.A. (2008): Characterization of natural feldspars by Raman spectroscopy for future planetary exploration. *The Canadia Mineralogist,* **46**, 1477-1500.

Gendrin, A., Mangold, N., Bibring, J.P., Langevin, Y., Gondet, B., Poulet, F., Bonello, G., Quantin, C., Mustard, J., Arvidson, R., LeMouélic, S. (2005): Sulfates in Martian layered Terrains: the OMEGA/Mars express view. *Science*, **307**, 1587-1591.

Hewins, H. *et al.* (2016): Regolith Northwes Africa 7533: Mineralogy and petrology with implications for early Mars. *Meteoritics & Planetary Science*, **52**, 89-124.

Hoehse, M., Mory, D., Florek, S., Weritz, F., Gornushkin, I., Panne, U. (2009): A combined laser-induced breakdown and Raman spectroscopy Echelle systemn for elemental and molecular microanalysis. *Spectrochimica Acta Part B: Atomic Spectroscopy*, **64**, 1219-1227.

27

Huang, E., Chen, C.H., Huang, T., Lin, E.H., and XU, J.-A. (2000): Raman spectroscopic characteristics of Mg-Fe-Ca pyroxenes. *American Mineralogist*, **85**, 473-479.

Jehlicka, J., Vitek, P., Edwards, H.G.M, Heagraves, M., Capoun, T. (2009): Application of portable Raman instruments for fast and non-destructive detection of minerals on outcrops. *Spectrochimica Acta Part A*, **73**, 410-419.

King, P.L., and McLennan, S.M. (2010): Sulfur on Mars. *Elements*, **6**, 107-112.

Knittle, E., Phillips, W., Williams, Q. (2001): An infrared and Raman spectroscopic study of gypsum at high pressures. *Physics Chemistry Mineral,* **28**, 630-640.

Kontoyannis, C.G., Orkoula, M.G., and Koutsoukos, P.G. (1997): Quantitative Analysis of Sulfated Calcium Carbonates Using Raman Spectroscopy and X-Ray Power Diffraction. *The Analyst*, **122**, 33-38.

Kolesov, B.A., and Tanskaya, J.V. (1996): Raman spectra and cation distribution in the lattice of olivines. *Materials Research Bulletin*, **31**, 1035-1044.

Kolesov, B.A., and Geiger, C.A. (2004): A Raman spectroscopic study of Fe-Mg olivines. *Physics and Chemistry Minerals*, **31**, 142-154.

28

657   Kristova, P., Hopkinson, L., Rutt, K., Hunter, H., and Cressey, G.

658   (2013): Quantitative analyses of powdered multi-minerallic

659   carbonate aggregates using a portable Raman spectrometer.

660   *American Mineralogist*, **98**, 401-409.

661   Kuebler, K.E., Jolliff, B.L., Wang, A., Haskin, L.A. (2006): Extractif

662   olivine (Fo-Fa) compositions from Raman spectral peak

663   positions. *Geochimica et Cosmichimica Acta,* **70**, 6201-6222.

664   Lodders, K. (1998): A survey of shergottite, nakhlite and chassigny

665   meteorites whlore-rock compositions. *Meteoritics & Planetary*

666   *Science*, **33**, 183-190.

667   Le Losq, C., Neuville, D.R, Moretti, R., Roux, J. (2012): Determination

668   of water content in silicate glasses using Raman spectrometry:

669   Implications for the study of explosive volcanism. *American*

670   *Mineralogist*, **97**, 779-790.

671   Mangold, N., Baratoux, D., Witasse, O., Encrenaz, T., Sotin, C. (2016):

672   Mars: a small terrestrial planet. *Astronomy and Astrophysics*

673   *Review,* **24**, 15.

674   Mangold, N., Schmidt, M.E., Fisk, M.R., Forni, O., McLennan, S.M.,

675   Ming, D.W., Sautter, V., Sumner, D., Williams, A.J., Clegg,

676   S.M., Cousin, A., Gasnault, O., Gellert, R., Grotzinger, J.P.,

677   Wiens, R.C. (2017): Classification scheme for sedimentary and

678   igneous rocks in Gale crater, Mars. *Icarus*, **284,** 1-17.

679   Maurice, S., Wiens, R.C., Saccoccio, M., Barraclough, B., Gasnault, O.,

680   and 65 more authors (2012): The ChemCam Instrument Suite on

681   the Mars Science Laboratory (MSL) Rover: Science objectives

682   and Mast Unit Description. *Space Science Reviews*, **170**, 167-227.

683   Maurice, S. *et al.* (2016): ChemCam activities and discoveries during

684   the nominal mission of Mars Science Laboratory in Gale crater,

685   Mars. *Journal of Analytical Atomic Spectrometry*, **31**, 863-889.

686   McKeown, D.A., Bell, M.I., and Caracas, R. (2010): Theoretical

687   determination of the Raman spectra of single-crystal forsterite

688   (Mg_2SiO_4). *American Mineralogist*, **95**, 980-986.

689   McMillan, P. (1984): Structural studies of silicate glasses and melts:

690   applications and limitations of Raman spectroscopy. *American

691   Mineralogist*, **69**, 622-644.

692   McSween, H.Y., Taylor, G.J., Wyatt, M.B. (2009): Elemental

693   Composition of the Martian Crust. *Science*, **324**, 736-739.

694   Mercier, M., Di Muro, A., Giordano, D., Métrich, N., Lesne, P.,

695   Pichavant, M., Scaillet, B., Clocchiatti, R., Montagnac, G. (2009):

696   Influence of glass polymerization and oxidation on micro-Raman

697   water analysis in alumino-silicate glasses. *Geochimica et

698   Cosmochimica Acta*, **73**, 197-217.

699   Meslin, P.-Y., Gasnault, O., Forni, O., Schröder, S., Cousin, A., and 55

700   more authors and the MSL Science Team (2013): Soil Diversity

30

701 and Hydration as Observed by ChemCam at Gale Crater, Mars.

702 *Science*, **341**.

703 Morizet, Y., Brooker, R.A., Iacono-Marziano, G., Kjarsgaard, B.A.

704 (2013): Quantification of dissolved CO_2 in silicate glasses using

705 micro-Raman spectroscopy. *American Mineralogist*, **98**, 1788-

706 1802.

707 Morizet, Y., Paris, M., Di Carlo, I., Scaillet, B. (2013): Effect of

708 Sulphur on the structure of silicate melts under oxidizing

709 conditions. *Chemical Geology*, **358**, 131-147.

710 Morizet, Y., Gennaro, E., Jego, S., Zajacz, Z., Iacono-Marziano, G.,

711 Pichavant, M., Di Carlo, I., Ferraina, C., Lesne, P. (2017): A

712 Raman calibration for the quantification of SO_4^{2-} groups

713 dissolved in silicate glasses: Application to natural melt

714 inclusions. *American Mineralogist*, **102**, 2065-2076.

715 Morrison, S.M. (2017): Crystal chemistry of martian minerals from

716 Bradbury Landing through Naukluft Plateau, Gale Crater, Mars.

717 *American Mineralogist, in press*.

718 Mustard, J.F., Poulet, F., Bibring, J.P., Langevin, Y., Gondet, B.,

719 Mangold, N., Bellucci, G., Altieri, F. (2005): Olivine and

720 pyroxene diversity in the crust of Mars. *Science*, **307**, 1594-1597.

721   Mysen, B.O., and Virgo, D. (1980a): Solubility mechanisms of carbon
722   dioxide in silicate melts: a Raman spectroscopic study. *American*
723   *Mineralogist*, **65**, 885-899.

724   Mysen, B.O., and Virgo, D. (1980b): The solubility behavior of CO_2 in
725   melts on the join $NaAlSi_3O_8$-$CaAl_2SiO_8$-CO_2 at high pressures
726   and temperatures: A Raman spectroscopic study. *American*
727   *Mineralogist*, **65**, 1166-1175.

728   Nachon, M. (2016) : Chimie de la surface de Mars dans le cratère Gale
729   par l'analyse de données élémentaires de ChemCam sur Curiosity
730   couplée à des simulations en laboratoire. PhD thesis.

731   Nachon, M., *et al.* (2017): Chemistry of diagnetic features analyzed by
732   ChemCam at Pahrump Hill, Gale crater, Mars. *Icarus*, **281**, 131-
733   136.

734   Noguchi, N., Shinoda, K., and Masuda, K. (2009): Quantitative analysis
735   of binary mineral mixtures using Raman microspectroscopy:
736   Calibration curves for silica and calcium carbonate minerals and
737   application to an opaline silica nodule of volcanic origin. *Journal*
738   *of Mineralogical and Petrological Sciences*, **104**, 253-262.

739   Ody, A. (2012): Dépouillement et interprétation des données spatiales
740   d'imagerie hyperspectrale de Mars (OMEGA/MEx): Evolution
741   volcanique de la surface de Mars. PhD thesis.

32

Ollila, A.M., *et al.* (2017): Preliminary Evaluation of the Mars 2020 Rover's SuperCam Development Unit: Co-Aligned Chemical and Mineralogical Analyses. *Lunar and Planetary Science XLVIII*.

Panczer, G., De Ligny, D., Mendoza, C., Gaft, M., Seydoux-Guillaume, A.-M., and Wang, X. (2012): Raman and fluorescence. *EMU Notes in Mineralogy*, **12**, 1-22.

Prencipe, M., Mantovani, L., Tribaudino, M., Bersani, D., Lottici, P.P. (2011): The Raman spectrum of diopside: a comparison between ab initio calculated and experimentally measured frequencies. *European Journal of Mineralogy*, **24**, 457-464.

Reynard, B., Montagnac, G., and Cardon, H. (2012): Raman spectroscopy at high pressure and temperature for the study of the Earth's mantle and planetary minerals. *EMU Notes in Mineralogy*, **12**, 365-388.

Rossano, S. and Mysen, B. (2012): Raman spectroscopy of Silicate Glasses and Melts. *EMU Notes in Mineralogy*, **12**, 319-364.

Rull, F. (2012): The Raman Effect and the vibrational dynamics of molecules and crystalline solids. *EMU notes in Mineralogy*, **12**, 1-60.

Sallé, B., Lacour, J-L., Vors, E., Fichet, P., Maurice, S., Cremers, D.A., Wiens, R.C. (2004) : Laser-Induces Breakdown Spectroscopy for Mars surface analysis : capabilities at stand-off distances and

764 detection of chlorine and sulfur elements. *Spectrochimica Acta*

765 *Part B: Atomic Spectroscopy*, **59**, 1413-1422.

766 Sautter, V. *et al*. (2015): In situ evidence for continental crust on early

767 Mars. *Nature Geosciences*, **8**, 605-609.

768 Sautter, V. *et al.* (2016): Magmatic complexity on early Mars as seen

769 through a combination of orbital, in-situ and meteorite data.

770 *Lithos*, **254-255**, 36-52.

771 Sharma, S.K., Simons, B., and Yoder Jr, H.S. (1983): Raman study of

772 anorthite, calcium Tschermak's pyroxene, and gehlnite in

773 crystalline and glassy states. *American Mineralogist*, **68**, 11-12.

774 Squyres, S.W., Knoll, A.H. (2005): Sedimentary rocks at Meridiani

775 Planum: Origin, diagenesis and implications for life on Mars.

776 *Earth Planetary Science Letters*, **240**, 1-10.

777 Stolper, E.M., and the MSL team (2013): The Petrochemistry of

778 Jake_M: Martian Mugearite. *Science,* **341**.

779 Tarcea, N., and Popp, J. (2012): Raman data analysis. *EMU Notes in*

780 *Mineralogy*, **12**, 195-228.

781 Taylor, S.R., McLennan, S.M. (2009): Planetary Crusts. *Cambridge*,

782 378.

783 Tribaudino, M., Mantovani, L., Bersani, D., and Lottici, P.P. (2012):

784   Raman spectroscopy of $(Ca,Mg)MgSi_2O_6$ clinopyroxenes.

785   *American Mineralogist,* **97**, 1339-1347.

786 Vaniman, D.T *et al.* (2017): Calcium Sulfates At Gale Crater And

787   Limitations On Gypsum Stability. *48th Lunar Planetary Science*

788   *Conference.*

789 Wang, A., Jolliff, B.L., Haskin, l.A., Kuebler, K.E., and Viskupic, K.M.

790   (2001): Characterization and comparison of structural and

791   compositional features of planetary quadrilateral pyroxenes by

792   Raman spectroscopy. *American Mineralogist*, **86**, 790-806.

793 Wang, A., Kuebler, K.E., Haskin, L.A. (2003): Raman spectroscopy

794   characterization of the feldspars – Implications for In situ surface

795   mineral characterization in planetary exploration. *Lunar and*

796   *Planetary Science XXXIV*.

797 Wiens, R.C. *et al.* (2012): The ChemCam Instrument Suite on the Mars

798   Science Laboratory (MSL) Rover: Body Unit and combined

799   System Tests. *Space Science Reviews*, **170**, 167-227.

800 Wiens, R.C., *et al.* (2016): SuperCam Remote-Sensig on the Mars 2020

801   Rover: Science Goals and Overview 3rd International Workshop

802   on Instrumentation for Planetary Missions. 4136.

803 Wray, J., Hansen, S.T., Dufek, J., Swayze, G.A., Murchie, S.L., Seelos,

804   F.P., Skok, J.R., Irwin III, R.P., Ghiorso, M.S. (2013): Prolonged

805   magmatic activity on Mars inferred from the detection of felsic

806   rocks. *Nature Geoscience*, **6**, 1013-1017.

807   Zajacz, Z., Halter, W., Malfait, W.J., Bachmann, O., Bodnar, R.J.,

808   Hirschmann, M.M., Mandeville, C.W., Morizet, Y., Müntener,

809   O., Ulmer, P., Webster, J.D. (2005): A composition-independent

810   quantitative determination of the water content in silicate glasses

811   and silicate melt inclusions by confocal Raman spectroscopy.

812   *Contributions to Mineralogy and Petrology*, **150**, 631-642.

813

814   **Figure captions:**

815   Figure 1: A: Pellet of a 90/10 mixture of olivine (weight fraction

816    $WF_{olivine} = 0.90$) and gypsum ($WF_{gypsum} = 0.10$) named GOLI90; B: 5

817   mm mapping of spectrum intensities acquired by Raman spectroscopy

818   showing the homogeneity of GOLI90; C: The average spectrum issued

819   from the 5 mm mapping of GOLI90 with v_1 peaks (symmetric stretching

820   mode of SiO_4 and SO_4 molecules) of olivine and gypsum reported.

821   Figure 2: Multi-minerallic pure Raman spectrum with their acquisition

822   time for A : olivine ; B: Mg-sulfate; C: gypsum; D: plagioclase; E:

823   clinopyroxene; and F: orthopyroxene. Significant peaks for each

824   minerals has been reported in graphs. For peak assignments see Table

825   2.

826

36

827 Figure 3: A: Global spectra for every mixtures of olivine with gypsum

828 in different proportions: A: $WF_{olivine}$ = 0.99; B: $WF_{olivine}$ = 0.95; C:

829 $WF_{olivine}$ = 0.90; D: $WF_{olivine}$ = 0.80; with their main peaks reported.

830 Variations of gypsum ν_1 (symmetric stretch of SO_4) peak intensity are

831 shown in red arrows. Zoom (890-1100 cm^{-1} area) of spectra acquired

832 by Raman spectroscopy after mapping, from different mixtures of

833 olivine with gypsum in several proportions: E: WF_{gypsum} = 0.01; F:

834 WF_{gypsum} = 0.05; G: WF_{gypsum} = 0.10; H: WF_{gypsum} = 0.20. Spectra are

835 correlated with peak simulations: blue for olivine peaks and green for

836 gypsum's. Red curves are cumulative peaks and black dotted lines are

837 residuals from simulations. Weight fractions are calculated with peak

838 simulations and reported in boxes in each graph and in Table 3.

839

840 Figure 4: Calibration coefficients calculated from simulated areas of

841 gypsum and mineral mixed versus the weight fraction (WF) of gypsum

842 theoretical. Black square are samples simulated with their relative

843 errors. Red lines correspond to calibration lines extrapolated from

844 calibration coefficients depending on theoretical weight fraction of

845 gypsum. Calibration lines established on four binary mixtures of: A:

846 plagioclase; B: orthopyroxene; C: clinopyroxene; D: olivine; with

847 gypsum in different proportions (WF_{gypsum} = 0.20, 0.10, 0.05, 0.03,

848 0.01). Equations and linear regression coefficient (R^2) of each

849 calibration lines are reported in boxes in each graph.

850

37

Figure 5: Calibration line for ternary mixtures of gypsum (WF$_{gypsum}$ =0.2, 0.1, 0.05) with olivine (WF$_{olivine}$ = 0.40, 0.50, 0.50) and clinopyroxene (WF$_{clinopyroxene}$ = 0.40, 0.40, 0.45). Black squares are simulations results with their errors (black vertical lines). Red line is the calibration line calculated from simulations results. Equation and regression linear coefficient (R^2) are specified in the graph box.

Figure 6: Calibration coefficients calculated from simulated areas of Mg-sulfate and mineral mixed versus the theoretical weight fraction (WF) of the sulfate. Black square are samples simulated with their relative errors. Red lines correspond to calibration lines extrapolated from calibration coefficients depending on theoretical weight fraction of Mg-sulfate. Calibration lines established on four binary mixtures of: A: orthopyroxene; B: plagioclase; C: clinopyroxene; D: olivine; with Mg-sulfate in different proportions (WF$_{gypsum}$ = 0.20, 0.10, 0.05 and 0.03). Equations and linear regression coefficients (R^2) of each calibration lines are reported in boxes for every graph.

Figure 7: Weight fractions calculated for sulfates (Ca and Mg-sulfate) depending on its theoretical weight fraction in each mixture of olivine, clinopyroxene, orthopyroxene and plagioclase. In black, gypsum binary samples are represented. Mg-sulfate mixtures are in blue in the figure. Red diamonds: ternary mixtures of gypsum.

38

875

876

877

878

879

880

881

882

883

884

885

886

887

888

889

890   **Tables :**

891

Mineral	Origin	Chemical formula
Olivine	Forsterite from Maar de Borée (France)	$Si_{1.00} Fe_{0.18} Mg_{1.78} Na_{0.01} O_4$
Clinopyroxene	Augite from Maar de Borée (France)	$Si_{1.78} Al_{0.23} Fe_{0.09} Mg_{0.95} Ca_{0.57} Na_{0.11}O_6$
Orthopyroxene	Enstatite from Maar de Borée (France)	$Si_{1.85} Al_{0.16} Fe_{0.16} Mg_{1.62} Ca_{0.02} Na_{0.02} O_6$
Plagioclase	Anorthite from a diorite of StillWater (USA)	$Si_{2.21} Al_{1.76} Fe_{0.01} Mg_{0.01} Ca_{0.85} Na_{0.16} O_8$
Gypsum	Synthetic calcium sulfate dehydrated from MERCK (Germany)	$CaSO_4 .(2H_2O)$
Mg-sulfate	Synthetic magnesium sulfate hydrated from LABOSI (France)	$MgSO_4 .(nH_2O)$

892

893   Table 1: Origins and chemical compositions of basaltic minerals (olivine,

894   pyroxenes and plagioclase, determined by Scanning Electron Microscopy

895   (SEM) analysis) and sulfates used in this study.

896

897

898

899

900

901

902

903

904

905

Raman shift (cm^{-1})	Mode assignments
Orthopyroxene [1], [2], [3], [4]	
225-325	Fe-O octahedron
375-490	Mg-O octahedron
650-750	Si-O v_3^{c}

800-1100	Si-O v_1[a]
Clinopyroxene [1], [2],[3], [4]	
230 and 327	M-O* stretching
255 and 360	Ca-O stretching
393	Mg-O stretch
665	Si-O-Si v_2[b]
1010	Si-O v_1
Olivine [5], [6], [7], [8]	
820	Si-O v_1
850	Si-O v_1
914	Si-O v_3
950	Si-O v_3
Plagioclase [9] and [3]	
200-400	Lattice modes
420-503	Al-O or Si-O v_1
900-1000	Si-O-Al v_3
> 1000	Si-O-Si v_3
Gypsum [10], [11], [12]	
400-500	SO_4 v_2
600-700	SO_4 v_4[d]
1006	SO_4 v_1
>1100	SO_4 v_3
Mg-sulfate [11]	
400 - 600	SO_4 v_2
620	SO_4 v_4
1040	SO_4 v_1
1050 – 1150	SO_4 v_3

906   [a] v_1: Symmetric stretch

907   [b] v_2: symmetric bending

908   [c] v_3: antisymmetric stretch

909   [d] v_4: antisymmetric bending

910   * With M referring as different metal cations present in the chemical structure

911   of the mineral (Buzgar et al. 2009)

912   Table 2: Specific peak assignments for each mineral used in this study.

913   Principal peaks observed in spectra are described according to [1]: Huang et

914   al. (2000), [2]: Prencipe et al. (2011), [3]: Sharma and al. (1983), [4]: Wang

915   et al. (2001) [5]: Chopelas (1991), [6]: Kolesov and Tanskaya (1996), [7]:

916   Kolesov and Geiger (2004), [8]: McKeown et al. (2010), [9]: Freeman et al.

917	(2008) [10]: Bishop et al. (2014), [11]: Buzgar et al. (2009) and [12]: Knittle		
918	et al. (2001).		

930   Table 3: Samples created in this study for binary and ternary mixtures with

931   sulfates (Ca and Mg) and basaltic minerals (i.e olivine, orthopyroxene,

932   clinopyroxene and plagioclase). Peak simulated in each mixture are reported,

933   followed by the calibration equation resulting from calibrations. Weight

934   fractions (WF) theoretical, WF calculated and coefficients (a) are reported for

935   each mixture. Errors relative to calculations are reported next to the WF

936   calculated and coefficients.

937

Sample name	WF theoretical	WF calculated	a
Olivine – Gypsum Peak simulated : 914 and 1006 cm^{-1}			

42

	Calibration equation : $a = 81.36 \times WF_{sulfate\ theoretical}$		
GOLI80	0.80 - 0.20	0.79 (0.08) – 0.21 (0.01)	17.21(3.20)
GOLI90	0.90 – 0.10	0.91 (0.01) – 0.09 (0)	6.55 (0.36)
GOLI95	0.95 – 0.05	0.94 (0.01) – 0.06 (0)	4.04 (0.22)
GOLI97	0.97 – 0.03	0.97 (0.02) – 0.03 (0.04)	1.87 (0.88)
GOLI99	0.99 – 0.01	0.99 (0) – 0.01 (0)	0.76 (0.08)
	Orthopyroxene - Gypsum		
	Peak simulated : 230 and 491 cm^{-1}		
	Calibration equation : $a = 8.23 \times WF_{sulfate\ theoretical}$		
GOPX80	0.80 – 0.20	0.85 (0.04) – 0.15 (0.03)	1.52 (0.01)
GOPX90	0.90 – 0.10	0.89 (0.03) – 0.11 (0.04)	0.99 (0.12)
GOPX95	0.95 – 0.05	0.94 (0.02) – 0.06 (0.05)	0.51 (0.01)
GOPX97	0.97 – 0.03	0.96 (0.01) – 0.04 (0.08)	0.34 (0.35)
GOPX99	0.99 – 0.01	0.98 (0.01) – 0.02 (0.05)	0.19 (0.23)
	Clinopyroxene – Gypsum		
	Peak simulated : 362 and 412 cm^{-1}		
	Calibration equation : $a = 1.93 \times WF_{sulfate\ theoretical}$		
GCPX80	0.80 – 0.20	0.82 (0.02) – 0.18 (0.02)	0.40 (0.49)
GCPX90	0.90 – 0.10	0.92 (0.01) – 0.08 (0.03)	0.15 (0.69)
GCPX95	0.95 – 0.05	0.93 (0) – 0.07 (0.01)	0.13 (0.38)
GCPX97	0.97 – 0.03	0.96 (0.01) – 0.04 (0.06)	0.07 (0.54)
GCPX99	0.99 – 0.01	0.99 (0) – 0.01 (0)	0.02 (0.42)
	Plagioclase - Gypsum		
	Peak simulated : 504 and 1006 cm^{-1}		
	Calibration equation : $a = 59.83 \times WF_{sulfate\ theoretical}$		
GPG80	0.80 – 0.20	0.83 (0.01) – 0.17 (0.01)	1.19 (0.02)
GPG90	0.90 – 0.10	0.90 (0.03) – 0.10 (0.01)	6.24 (0.89)
GPG95	0.95 – 0.05	0.95 (0.01) – 0.05 (0)	2.75 (0.10)
GPG97	0.97 – 0.03	0.98 (0.01) – 0.02 (0.01)	1.17 (0.04)
GPG99	0.99 – 0.01	0.98 (0) – 0.02 (0)	1.15 (0.01)
	Olivine – Clinopyroxene - Gypsum		
	Peak simulated : 947 - 310/328/359/384 - 485		
	Calibration equation: $a = 1.71 \times W_{sulfate\ theoretical}$		
GOLCX80	0.40 – 0.40 – 0.20	0.35 (0.27) – 0.50 (0.01) – 0.15 (0.06)	0.35 (0.05)
GOLCX90	0.50 – 0.40 – 0.10	0.49 (0.16) – 0.35 (0.06) – 0.05 (0.03)	0.15 (0.03)
GOLCX95	0.50 – 0.45 – 0.05	0.39 (0.17) – 0.44 (0.07) – 0.03 (0.03)	0.07 (0.02)

938

939

940

941

942

943

944

Sample name	WF theoretical	WF calculated	a

	Olivine - Mg-sulfate		
	Peak simulated : 950 and 1040 cm^{-1}		
	Calibration equation: a= 5.26 x WF$_{sulfate\ theoretical}$		
MgOLI80	0.80 - 0.20	0.84 (0.05) - 0.16 (0.09)	0.90 (0.19)
MgOLI90	0.90 - 0.10	0.86 (0.02) - 0.14 (0.03)	0.81 (0.03)
MgOLI95	0.95 - 0.05	0.94 (0.03) - 0.06 (0.19)	0.30 (0.59)
MgOLI97	0.97 – 0.03	0.95 (0.02) – 0.05 (0.20)	0.23 (0.63)
	Orthopyroxene - Mg-sulfate		
	Peak simulated: 330/370/400 - 1040 cm^{-1}		
	Calibration equation: a = 2.19 x WF$_{sulfate\ theoretical}$		
MgOPX80	0.80 - 0.20	0.82 (0.02) - 0.18 (0.02)	0.43 (0.02)
MgOPX90	0.90 - 0.10	0.89 (0.01) - 0.11 (0.02)	0.25 (0)
MgOPX95	0.95 - 0.05	0.90 (0.01) - 0.10 (0.02)	0.20 (0)
MgOPX97	0.97 – 0.03	0.96 (0) – 0.04 (0.01)	0.08 (0)
	Clinopyroxene - Mg-sulfate		
	Peak simulated: 666/1006 and 1040 cm^{-1}		
	Calibration equation: a = 1.05 x WF$_{sulfate\ theoretical}$		
MgCPX80	0.80 - 0.20	0.82 (0) – 0.18 (0.04)	0.19 (0.01)
MgCPX90	0.90 - 0.10	0.87 (0) – 0.13 (0.03)	0.14 (0.01)
MgCPX95	0.95 - 0.05	0.94 (0) – 0.06 (0.04)	0.06 (0.01)
MgCPX97	0.97 – 0.03	0.96 (0) – 0.04 (0.03)	0.03 (0.01)
	Plagioclase - Mg-sulfate		
	Peak simulated: 750 and 1113 cm^{-1}		
	Calibration equation: a = 2.88 x WF$_{sulfate\ theoretical}$		
MgPG80	0.80 - 0.20	0.86 (0.04) – 0.14 (0.09)	0.51 (0.15)
MgPG90	0.90 - 0.10	0.91 (0.03) – 0.09 (0.12)	0.33 (0.21)
MgPG95	0.95 - 0.05	0.93 (0.01) – 0.07 (0.07)	0.23 (0.11)
MgPG97	0.97 – 0.03	0.93 (0.02) – 0.07 (0.06)	0.22 (0.10)

945

946   Table 3 (suite)

947

948

949

950

951

A

GOLI90
$WF_{olivine} = 0.90$
$WF_{gypsum} = 0.10$
8 mm-pellet

2 mm

B 5 mm mapping on GOLI90
Raman maximum intensities map

2 mm

C GOLI90 spectrum

υ_1 olivine
814,850,901,920 cm^{-1}

υ_1 gypsum
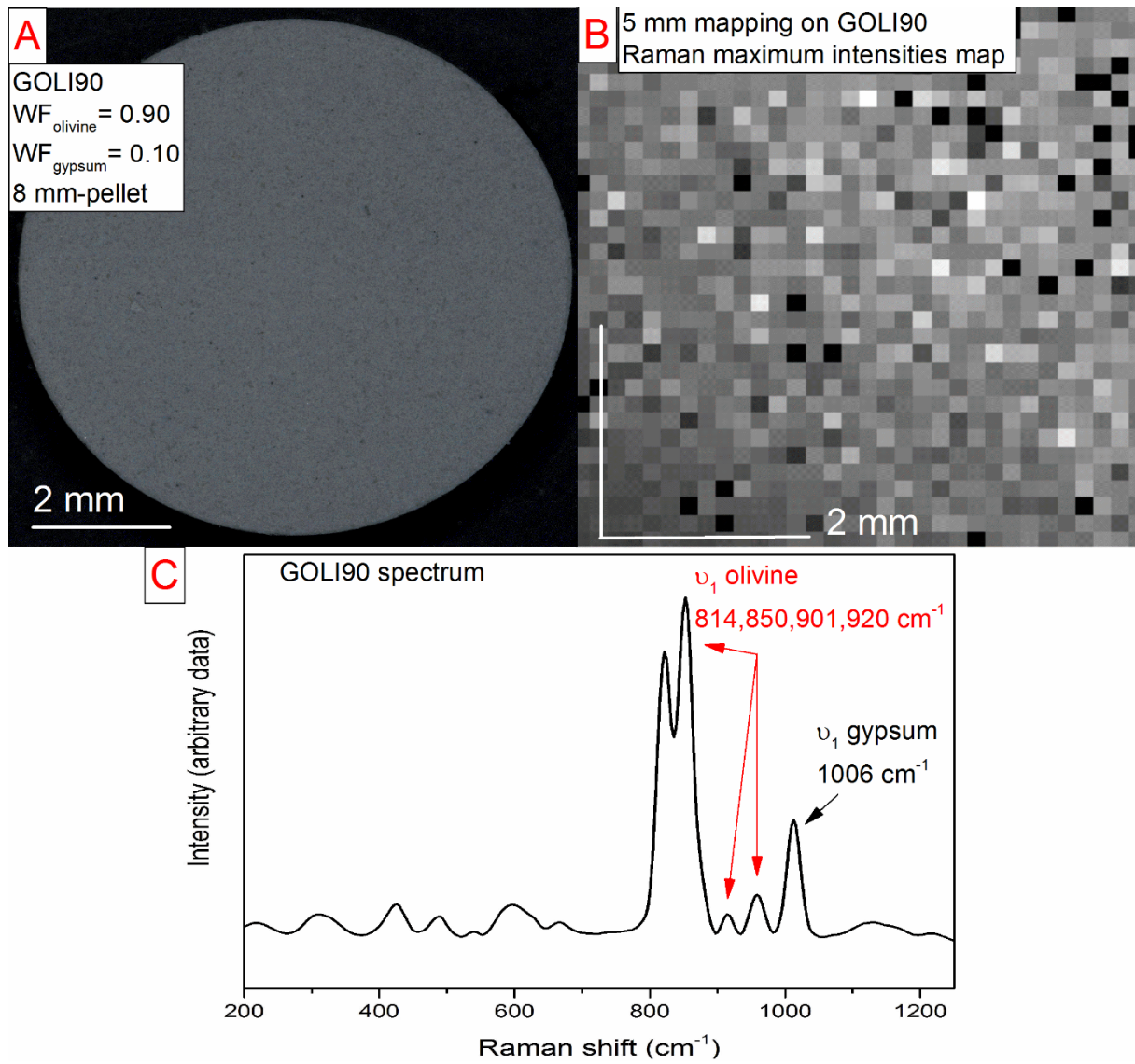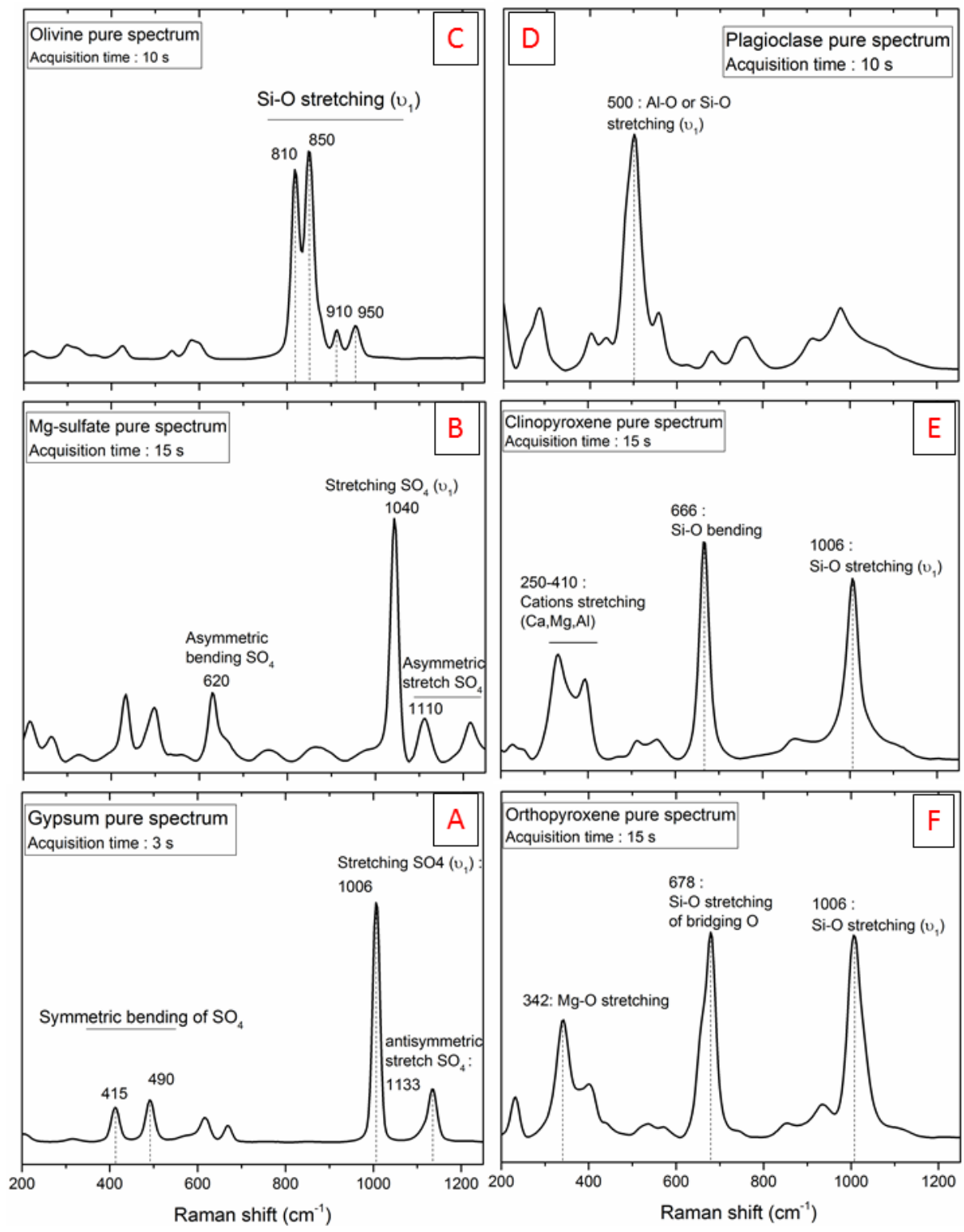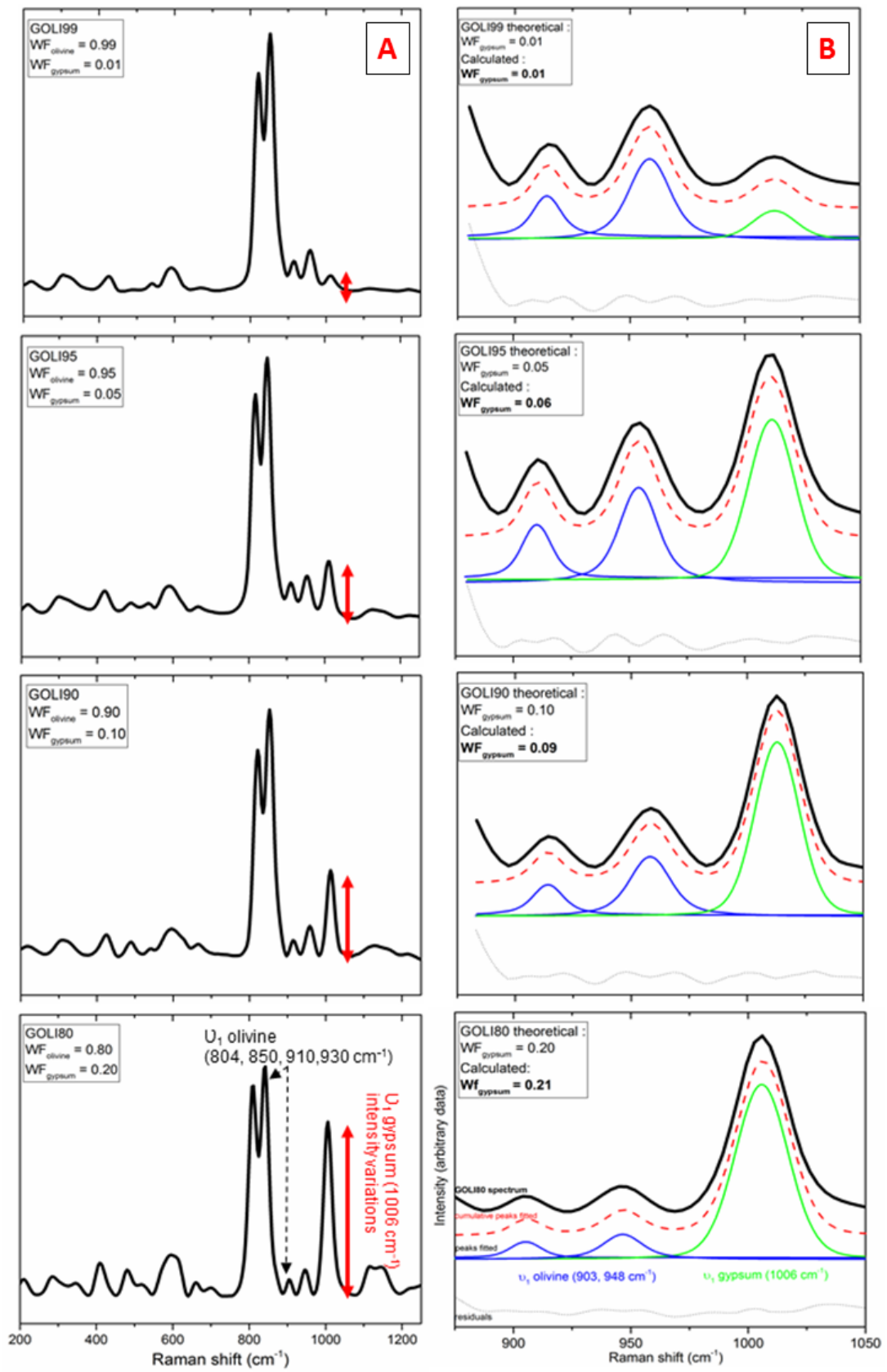1006 cm^{-1}

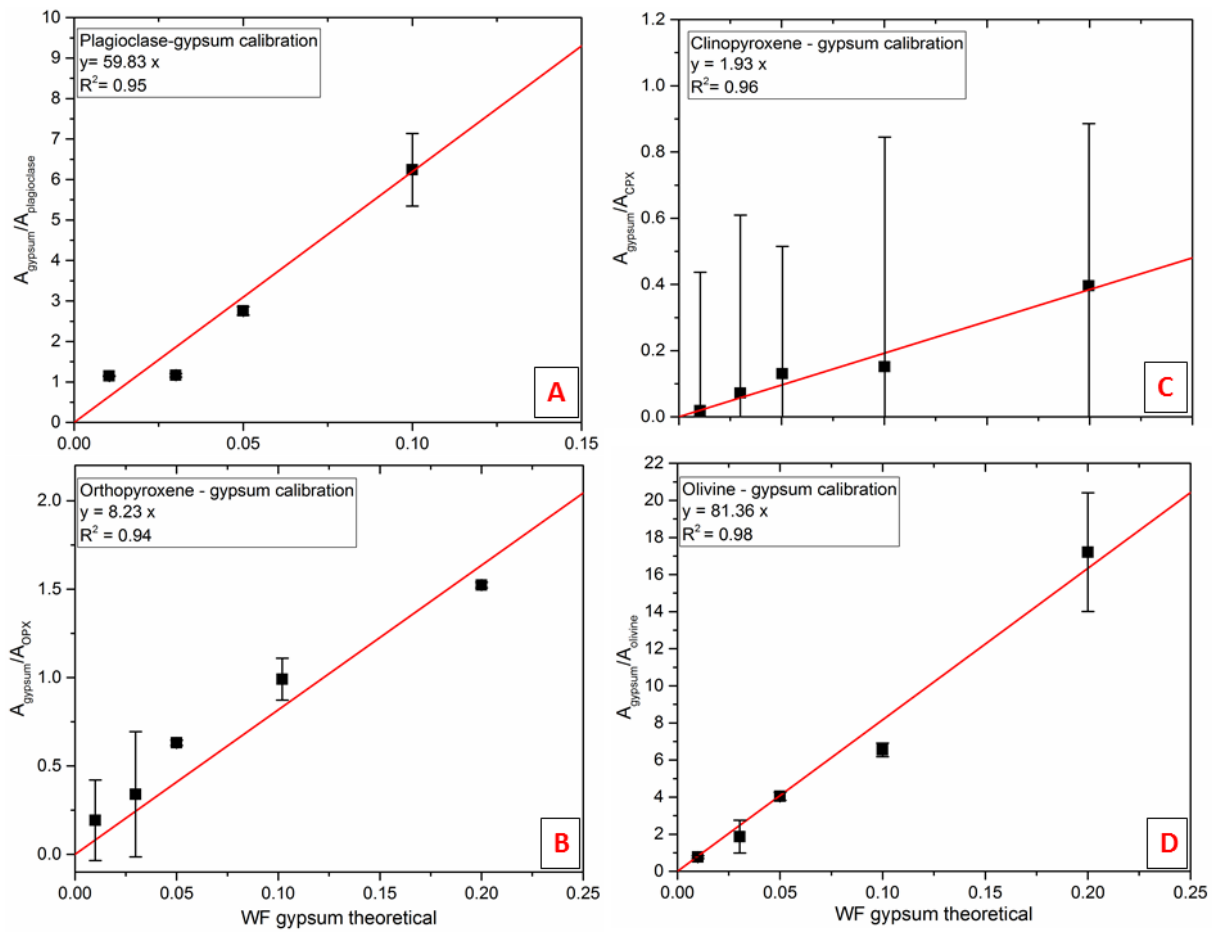Intensity (arbitrary data)

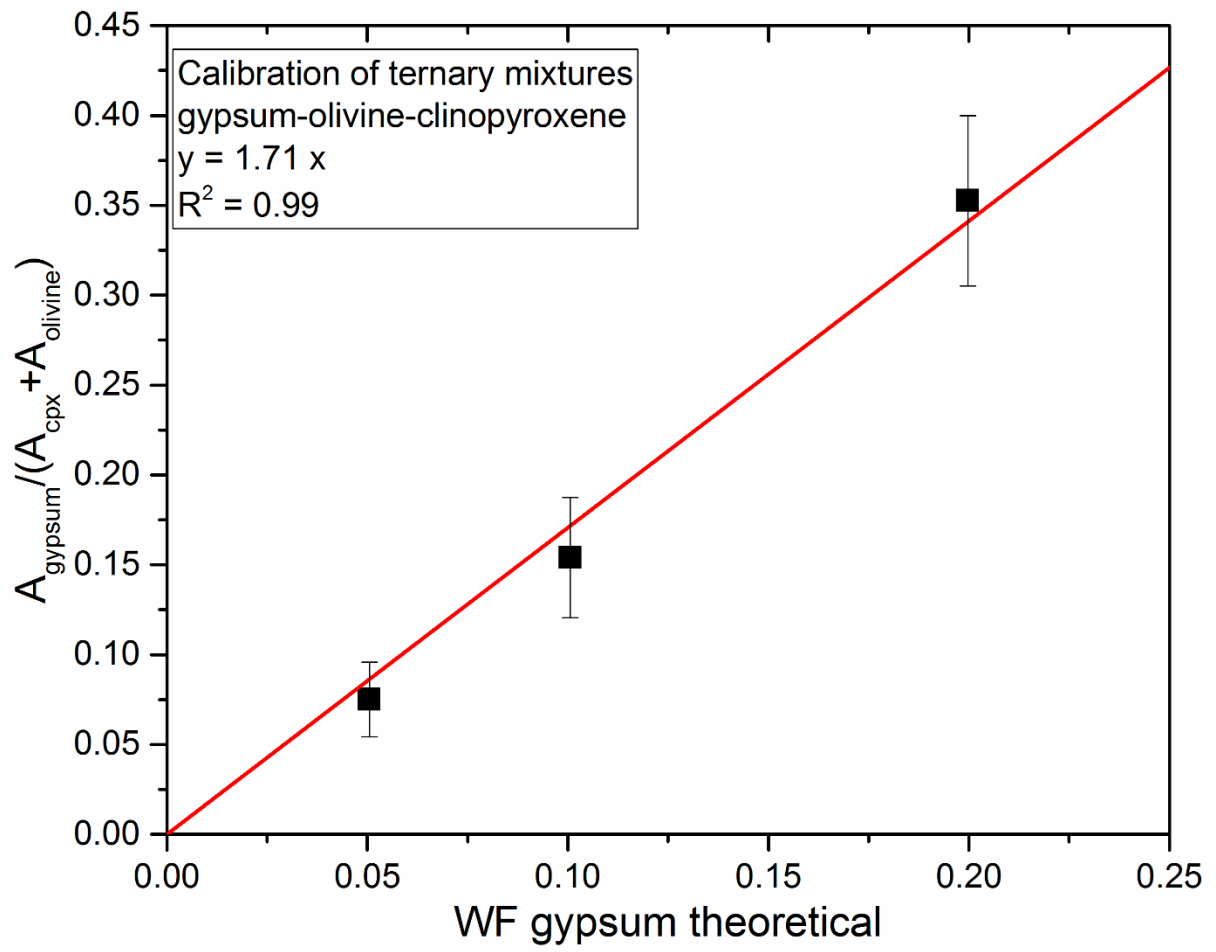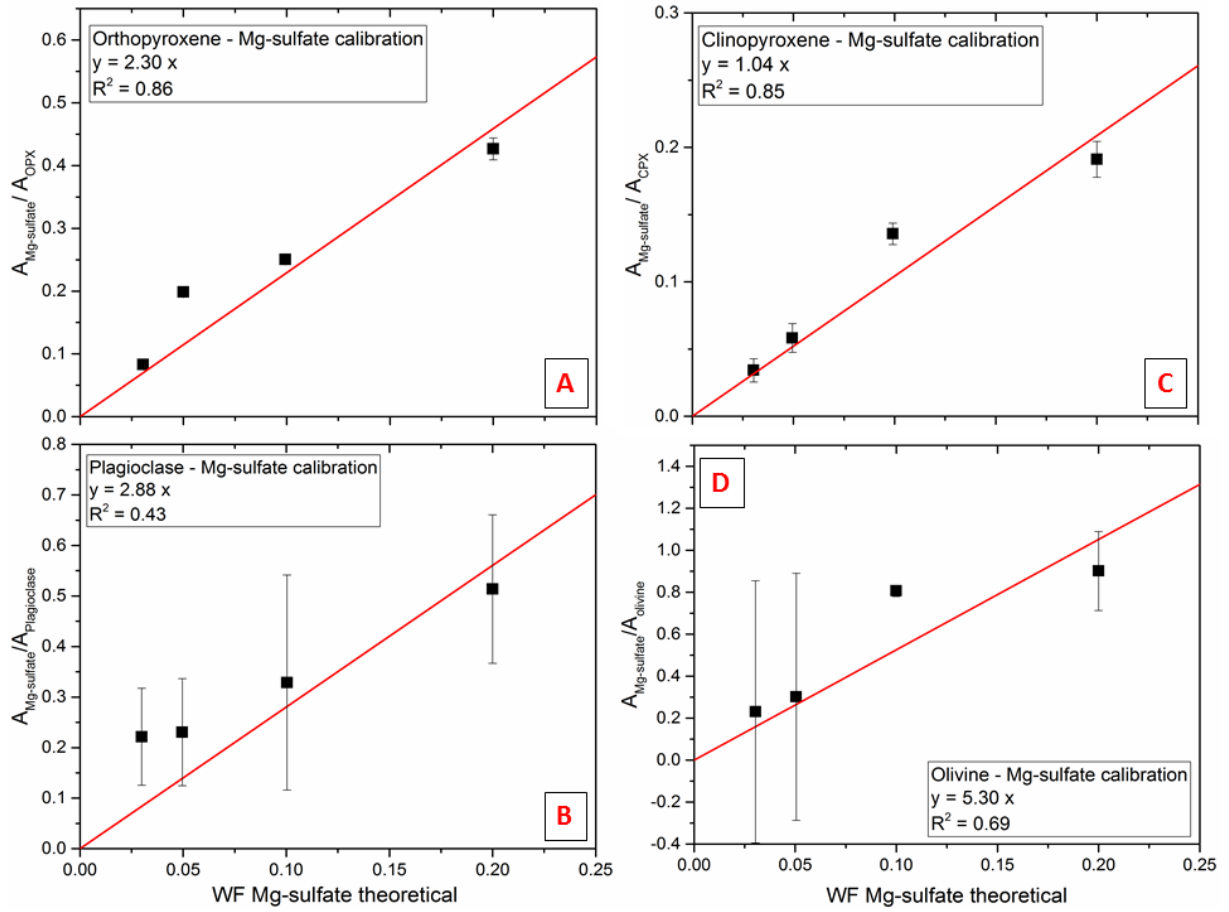Raman shift (cm^{-1})

Figure 1

Figure 2

Figure 3

Figure 4

Figure 5

Figure 6

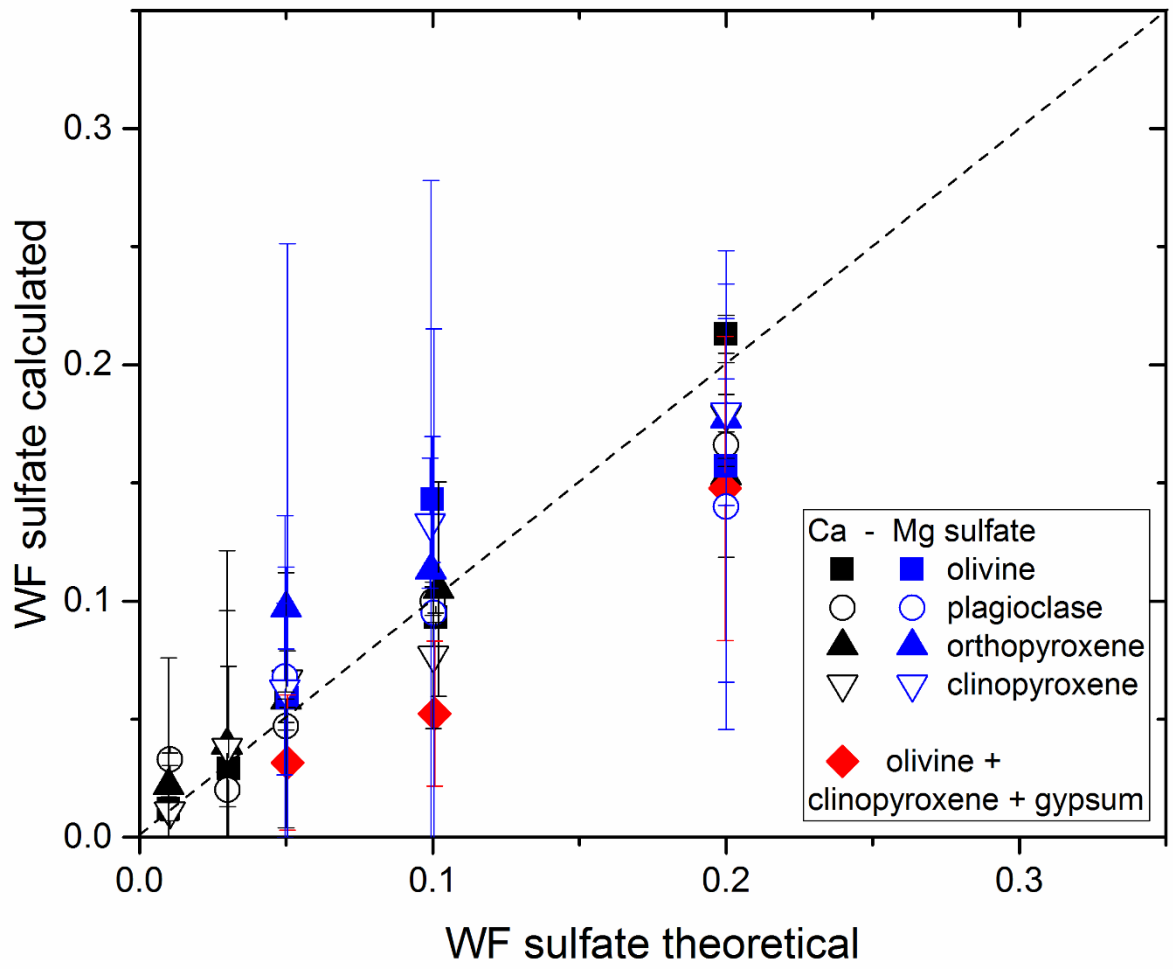Figure 7

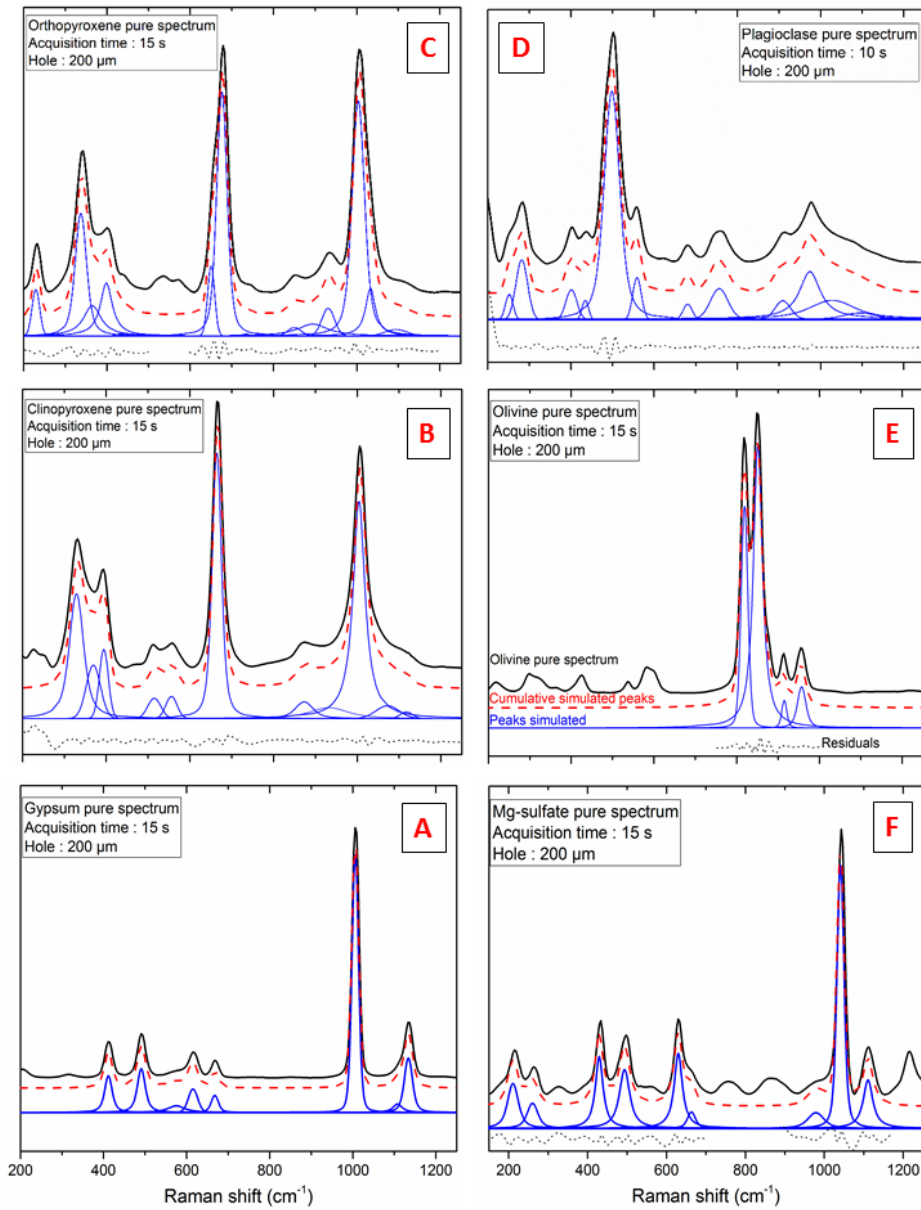**Supplementary material:**

Figure caption:

Figure 1: Deconvolution of minerals pure spectrum for A: gypsum; B: clinopyroxene; C: orthopyroxene; D: plagioclase; E: olivine; and F: Mg-sulfate. With individual peaks simulated in blue, cumulative peaks simulated in red dashed lines and residuals in black dotted lines. Analytical parameters (acquisition time and confocal mode) are described for each spectrum.
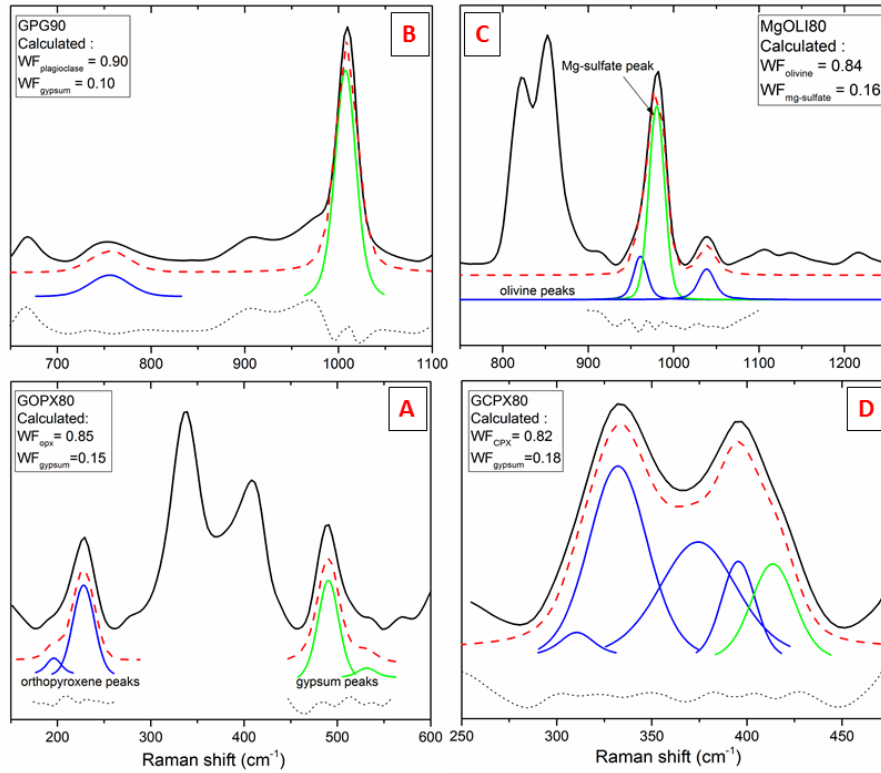
Figure 2: Peak simulations for the other different mixtures: A: orthopyroxene-gypsum mixture with initial proportion of 0.8 and 0.2 respectively; B: plagioclase-gypsum mixture with theoretical proportions of 0.9 and 0.1; C: olivine-mgsulfate mixture (theoretical proportions: $WF_{olivine}=0.8$ and $WF_{Mg-sulfate}=0.2$); D: clinopyroxene-gypsum mixture of theoretical weight fraction of 0.90 and 0.10 respectively. Green peaks are attributed to sulfates vibrations (Ca or Mg) and blue ones for silicate minerals. Red dashed and blacks dotted lines are cumulative peaks simulated and residuals left after simulations. Weight fraction calculated by simulations for examples shows in this figure are reported in each graph. All results from simulations on the different mixtures are described in **Table 4**.